Parameter Analysis of Millimeter-Wave Waveguide Switch Based on a MEMS-Reconfigurable Surface

Zargham Baghchehsaraei, *Student Member, IEEE*, and Joachim Oberhammer, *Senior Member, IEEE*

***Abstract*—This paper presents a novel concept of a millimeter-wave waveguide switch based on a microelectromechanical (MEMS)-reconfigurable surface with insertion loss and isolation very similar to high performance but bulky rotary waveguide switches, despite its thickness of only 30 μm. A set of up to 1470 micromachined cantilevers arranged in vertical columns are actuated laterally by on-chip integrated MEMS comb-drive actuators, to switch between the transmissive state and the blocking state. In the blocking state, the surface is reconfigured so that the wave propagation is blocked by the cantilever columns short-circuiting the electrical field lines of the TE_{10} mode. A design study has been carried out identifying the performance impact of different design parameters. The RF measurements (60–70 GHz) of fabricated, fully functional prototype chips show that the devices have an isolation between 30 and 40 dB in the OFF state and an insertion loss between 0.4 and 1.1 dB in the ON state, of which the waveguide-assembly setup alone contributes 0.3 dB. A device-level yield analysis was carried out, both by simulations and by creating artificial defects in the fabricated devices, revealing that a cantilever yield of 95% is sufficient for close-to-best performance. The actuation voltage of the active-opening/active-closing actuators is 40–44 V, depending on design, with high reproducibility of better than ($\sigma = 0.0605$ V). Lifetime measurements of the all-metal, monocrystalline-silicon core devices were carried out for 14 h, after which 4.3 million cycles were achieved without any indication of degradation. Furthermore, a MEMS-switchable waveguide iris based on the reconfigurable surface is presented.**

***Index Terms*—Microelectromechanical (MEMS) components and techniques, MEMS switches, microwave switch, millimeter-waves, reconfigurable surface, Radio frequency MEMS (RF MEMS), waveguide switch.**

I. Introduction

THE millimeter-wave spectrum, historically mainly exploited for defense applications and radio astronomy, is of increasing interest for civilian applications, including cross-link communications between satellites [1], small-cell cloud networks [2], high speed wireless communication at 60 GHz [3] and E-band (71–76 GHz, 81–86 GHz) [4], automotive radar at 76–81 GHz [5], remote sensing at 94 GHz [6], medical imaging [7], and medical diagnosis [8]. Advantages of going to higher frequencies are larger available bandwidths, higher spatial resolution, better discrimination between materials, and smaller antenna and sensor interfaces [9]–[11].

Waveguide technology is superior to transmission lines in terms of loss and power handling. In order to make full advantage of waveguide technology, components inserted in the waveguide should be of equally low loss.

Conventional waveguide switches comprise mainly two concepts. First, rotary motor-based mechanical switches [12] have very low insertion loss and high isolation, but they are heavy, bulky, very slow and require high power for switching. Second, PIN-diode switched waveguide irises [13] which are switching in nanoseconds but have poor insertion loss/isolation performance and need relatively high biasing currents.

Radio frequency microelectromechanical systems (RF MEMS) technology has widely been attracting interest in recent decades as it offers the potential to replace other RF technologies due to near-ideal performance, such as high linearity, low loss, very small size, fast response, near-zero power consumption by electrostatic actuation, semiconductor compatibility, and high-volume manufacturability [14], [15].

Radio frequency microelectromechanical systems (RF MEMS) switches, including contact [16]–[18] and capacitive [19]–[22] type, have been developed since their introduction in 1991 [23] to very mature RF components [24]–[26]. Potentially, RF MEMS technology could combine the advantages of an electromechanical rotary switch with the advantages of a PIN diode switch, as summarized in Table I. However, to the knowledge of the authors, there have only been two attempts by another research group to build a MEMS waveguide switch; one was implemented with electrothermal actuators, with insertion loss of 1–2.8 dB and return loss of 15 dB in the Ku- and K-bands [27], and another one with electrostatic actuators, with an insertion loss of 0.9–1.2 dB and return loss of 20 dB over 7% of the Ku-band [28].

This paper presents a parameter analysis and device-level yield study of a new concept of a MEMS-based rectangular waveguide switch, implemented for E-band (60–90 GHz) and consisting of a MEMS reconfigurable surface integrated in a WR-12 waveguide and fabricated using a two-mask silicon-on-insulator (SOI) RF MEMS fabrication process flow based on a process originally developed by the authors for coplanar transmission line devices [29]. The authors have shown the basic idea of the waveguide switch in [30] and [31], though there the MEMS devices were not functionally working and the characterization was done on fixed hard-wired structures. This paper is an extension to IMS2013 conference paper [32], where, for the first time, we report on a fully -functional RF MEMS waveguide switch based on a large-scale

Manuscript received July 06, 2013; revised October 08, 2013; accepted October 16, 2013. Date of publication November 12, 2013; date of current version December 02, 2013. This paper is an expanded paper from the IEEE International Microwave Symposium, Seattle, WA, USA, June 2–7, 2013.

The authors are with the Department of Micro and Nanosystems, School of Electrical Engineering, KTH Royal Institute of Technology, Stockholm SE-100 44, Sweden (e-mail: zargham@kth.se; joachim.oberhammer@ee.kth.se).

Color versions of one or more of the figures in this paper are available online at http://ieeexplore.ieee.org.

Digital Object Identifier 10.1109/TMTT.2013.2287682

TABLE I
COMPARISON OF DIFFERENT TECHNOLOGIES FOR MILLIMETER-WAVE WAVEGUIDE SWITCHES

	rotary motor	**PIN diode**	**RF MEMS**
insertion loss	$<$ 0.3–0.8 dB [31]	$<$ 2.0–6.5 dB [31]	*as good as rotary motors due to mechanical switching nature of MEMS*
isolation	$>$ 40 dB [31]	$>$ 20 dB [31]	*as good as rotary motor switches*
speed	$\approx$ 100 ms (slow)	ns (fast)	*μs (medium speed)*
power consumption	high	medium	*very low (e.g. electrostatic actuation)*
volume	bulky	compact	*compact*
weight	heavy	light	*light*
reliability	high	high	*requires a reliable design concepts [33]–[35]*

MEMS-reconfigurable surface consisting of up to 1470 reconfigurable cantilever elements with up to 770 simultaneously switched contact points for short-circuiting the electric field lines of the TE_{10} mode of a WR-12 rectangular waveguide. This extended work discusses the waveguide switch in detail with a parameter analysis aiming for optimizing the number of contact points, compares different distributions of the elements of the reconfigurable surface, presents new measurement data, carries out a device-level yield analysis with measurements of yield-implications on the performance, and presents for the first time an implementation with measurement data of a switchable waveguide iris based on a MEMS-reconfigurable surface.

II. CONCEPT

The waveguide switch presented in this paper is based on a MEMS-reconfigurable surface that is inserted perpendicularly to the wave propagation into the waveguide. The surface consists of distributed metallized elements, which can be reconfigured by on-chip MEMS actuators outside the waveguide cross-section so that they are either blocking or not blocking the TE_{10} mode wave propagation in the waveguide.

A simplified schematic drawing of the single-pole single-throw (SPST) waveguide switch integrated in a WR-12 rectangular waveguide (inner dimensions 3.099 mm $\times$ 1.549 mm, 60–90 GHz) is shown in Fig. 1(a). The reconfigurable surface consists of a number of vertical columns that are split into smaller sections (vertical cantilevers) grouped into a set of fixed and a set of movable cantilevers. The fixed set is anchored at the narrow waveguide sidewalls, and the movable set is mechanically connected via horizontal suspension bars to electrostatic comb-drive push–pull MEMS actuators placed on-chip outside of the narrow sides of the waveguide. The MEMS actuators provide synchronous lateral movement of the vertical cantilevers. In the ON state (nonblocking), shown in Fig. 1(b), the vertical cantilevers of the fixed and moving elements are not in contact and thus allow the electromagnetic wave to propagate freely through the transmissive surface. In the OFF state, shown in Fig. 1(c), the movable vertical cantilevers are laterally moved into contact with the nonmovable vertical cantilevers, to form closed vertical columns which are blocking the wave propagation through the surface as they are short-circuiting the electric field lines of the dominant TE_{10} mode. The reconfigurable surfaces of the waveguide switches implemented in this paper are only 30 μm thick and thus provide minimum insertion loss in the transmissive state and very high isolation in the blocking state.

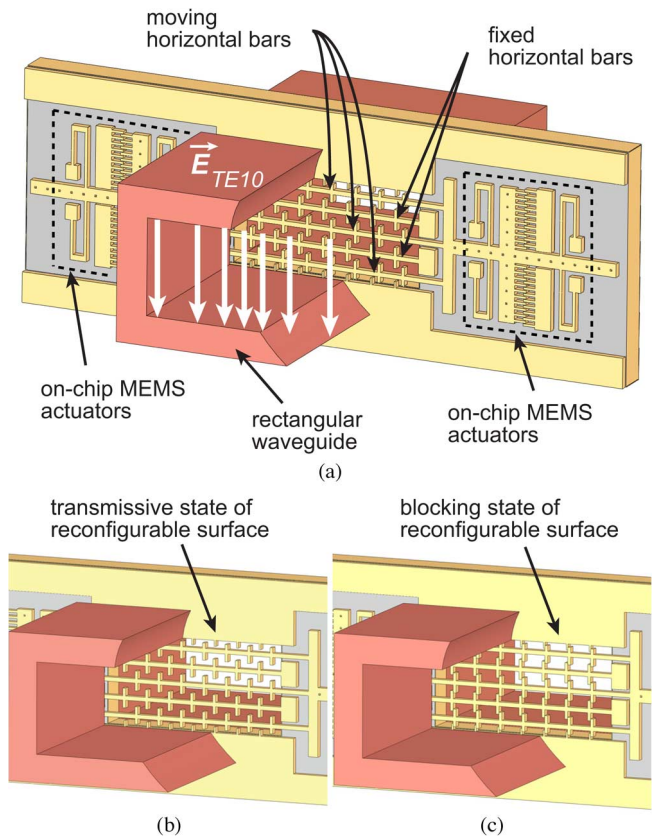

Fig. 1. Concept of presented MEMS waveguide switch. (a) Schematic view of switch drawn for three moving and two fixed horizontal suspension bars and seven cantilever columns (resulting in 42 contact points and 70 cantilevers). (b) ON state and (c) OFF state of the waveguide switch.

III. DESIGN STUDY AND PARAMETER ANALYSIS OF WAVEGUIDE SWITCH

The waveguide-switch performance in the blocking and nonblocking states is determined by the number of vertical columns and the number of sections of the columns, i.e., the number of horizontal suspension bars with associated vertical cantilevers, and on the distribution of these elements in the cross section of the waveguide.

This design study is based on simulations with ANSYS High Frequency Structural Simulator (HFSS) where the reconfigurable surface elements are modeled as gold blocks with a finite

resistivity of 2.049 $\mu\Omega$ – cm, as compared with gold-covered silicon blocks of the fabricated chips. The simulation model takes metal losses into account and includes a total (copper) waveguide length of 2.03 mm. The width (horizontal) and thickness (in direction of the wave propagation) of the contact cantilevers are 5 and 30 μm, respectively, with 5-μm vertical overlap between the moving and fixed vertical cantilevers to create a contact in the OFF state and with a 24-μm large horizontal gap in the ON state. The width (vertical) of the horizontal suspension bars is 25 μm, and the horizontal suspension bars are fully metallized. The simulation model includes all vertical cantilever elements and all horizontal suspension bars as for the fabricated devices, and mechanical feedthroughs in the narrower waveguide walls of the same geometry as in the final mask layout. The HFSS simulation model in the blocking state is shown in Fig. 2(a).

A. Uniform Distribution of Cantilever Columns

Fig. 2 shows the HFSS-simulated RF performance of the waveguide switch for the uniform distribution of contact cantilevers along the wide wall of the waveguide, with the number of horizontal suspension bars and vertical cantilever columns as parameters, at 75 GHz (E-band center frequency).

Increasing the number of vertical cantilever columns improves the blocking of the wave propagation and thus the OFF-state isolation, but impacts negatively the ON-state insertion loss. Since the horizontal suspension bars are perpendicular to the electric field lines inside the waveguide, they have a very weak effect on the RF performance of the structure even in the ON state, even if completely metallized such as for the waveguide-switch implementations of this paper. Furthermore, the more vertical cantilever sections in a column the less fraction of the wave is reflected in the ON state. More horizontal bars results in shorter vertical cantilevers and thus a higher degree of splitting of the sections which are intended to short-circuit the electric field lines in the blocking state. This results in lower insertion loss in the nonblocking state. Thus, if a larger number of vertical columns is desired to increase the isolation of the switch, the degradation in insertion loss can be compensated by also increasing the number of horizontal suspension bars. There is a saturation effect, i.e., increasing the number of horizontal suspension bars beyond a certain number, for instance 17 for 20 vertical columns, does not significantly improve the insertion loss. A combination of 20 vertical columns with 21 intersections (horizontal suspension bars) was found to achieve an optimum compromise in performance between the ON and the OFF state, resulting in an ON-state insertion loss and return loss better than 0.035 and 22.55 dB, respectively, and OFF-state isolation and reflected power better than 28.49 and 0.023 dB, respectively, for a total of 840 vertical cantilevers and 440 contact points. In conclusion, the blocking quality of the switch is determined by the number of vertical columns and weakly depending on the number of horizontal suspension bars, whereas the transmissive properties of the switch are dependent on the ratio of the horizontal bars to the vertical columns.

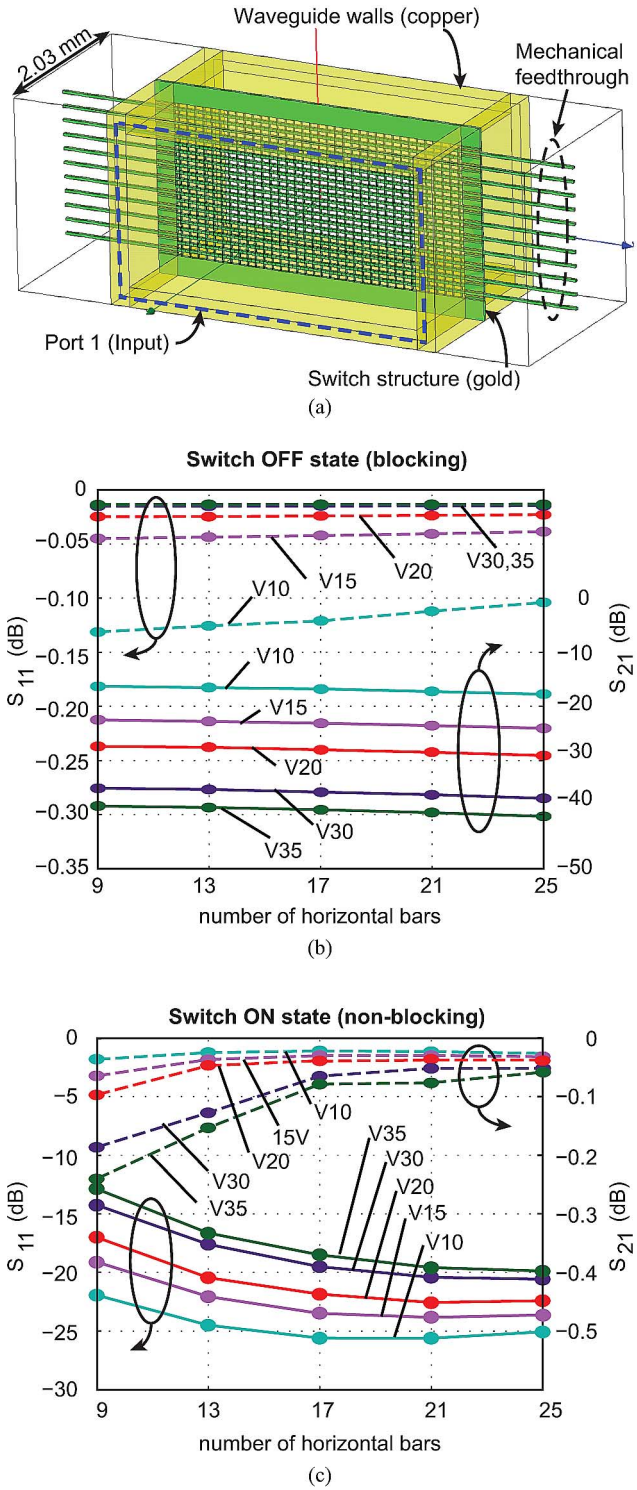

Fig. 2. HFSS design parameter study, investigating the RF performance at 75 GHz with dependence on the number of horizontal suspension bars with the number of vertical cantilever columns as parameter. (a) HFSS model for the switch with 21 horizontal bars and 35 vertical columns in the OFF state (blocking). Simulation results: (b) OFF state (blocking) and (c) ON state (nonblocking).

B. Optimized Distribution of Cantilever Columns

The density of the electric field lines of the dominant TE_{10} mode has a sinusoidal distribution along the horizontal axis of the rectangular waveguide cross section with a maximum at the center [36]. Thus, in addition to the number of rows

and columns, the distribution of the cantilever columns in the waveguide cross-section has influence on the performance. A sinusoidal distribution of the vertical columns is expected to result in improved OFF-state isolation at the same number of columns or allows for having similar OFF-state isolation at a reduced number of vertical columns and thus improved ON-state performance.

Fig. 3 shows the HFSS-simulated comparison among five structures while varying the number and distribution of vertical columns while keeping all other parameters identical (in particular: 17 horizontal bars). Structure 1 has 20 cantilever columns uniformly distributed, while for Structure 2 two cantilever columns are removed on each side, keeping the 16 central cantilever columns with the same spacing as in Structure 1. Structure 3 has uniformly distributed 16 cantilever columns. For Structures 4 and 5, the cantilever columns are following a sinusoidal distribution with highest density in the middle of the waveguide. Structure 4 has 16 cantilever columns, where the central cantilever density corresponds to the density of 20 uniformly distributed columns, and the cantilever density on the edges corresponds to the density of 16 uniformly distributed columns. Structure 5 has only 14 cantilevers, where the column density in the center corresponds to the density of a uniform distribution with 35 columns, and the density at the edges corresponds to a density of 14 columns. Drawings of the distributions of the cantilever columns of these five structures are shown in Fig. 3(c). The simulation results [Fig. 3(a) and 3(b)] show, that for Structure 2, removing a total four cantilever columns and thus decreasing the total number of columns by 20%, has negligible effect on the performance. The structure with 14 sinusoidally distributed cantilevers (30% decrease in the number of contact cantilevers as compared to the structure with 20 cantilever columns) and highest column density in the center performs clearly better than the uniform distribution of 16 cantilevers. As a conclusion, as expected, the important factor is the column density in the center, and a nonuniform distribution can substantially decrease the number of contact points with just slight decrease in the performance.

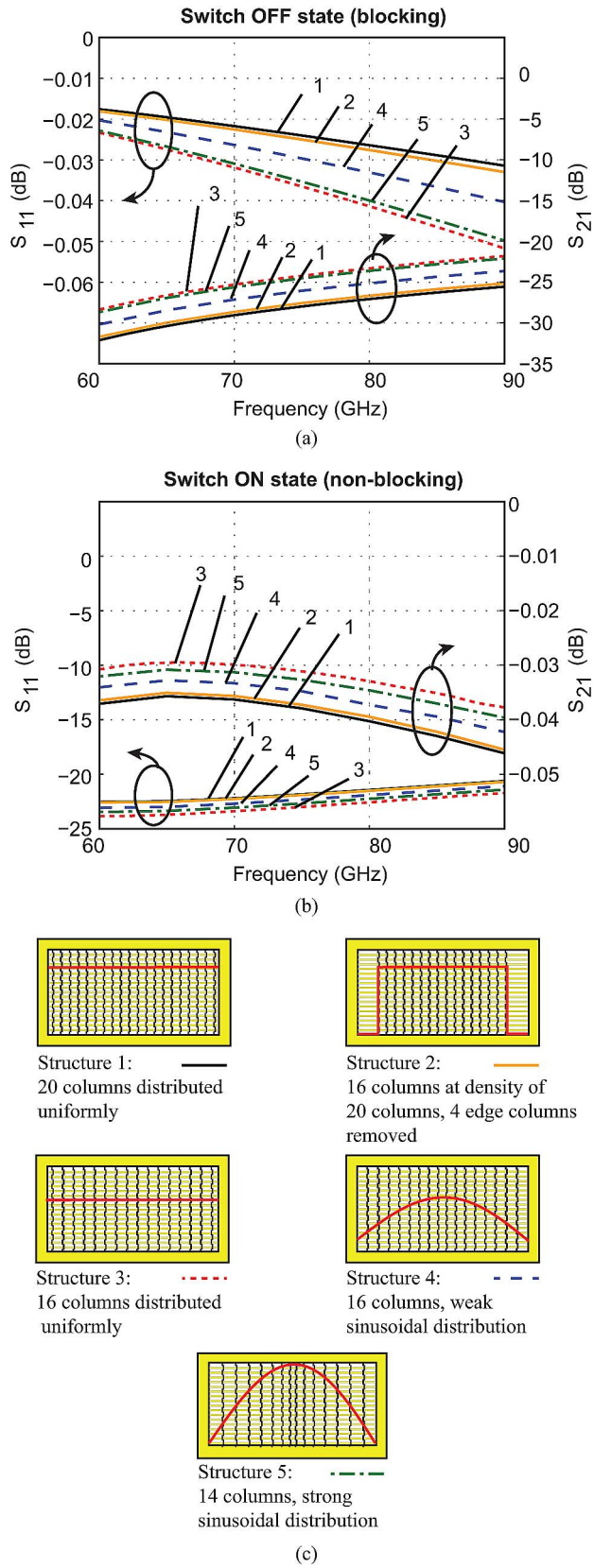

FIG. 3. HFSS-simulated study of the influence of the distribution of cantilever columns shown for five structures: (a) OFF state and (b) ON state. (c) Schematics of the investigated structures with the red line indicating the distribution of the column density.

IV. Fabrication and Measurement Setup

The three-dimensional (3-D) micromachined reconfigurable surface of the waveguide switches and irises are fabricated in a two-mask SOI RF MEMS micromachining process as outlined in Fig. 4.

Since the whole chip, including top and bottom faces and sidewalls, is finally completely covered with gold, there is no need to use a high-resistivity wafer and an SOI wafer with resistivity of 1–20 Ω – cm with device layer thickness of 30 μm, a buried oxide layer of 2 μm, and a handle wafer thickness of 450 μm is used. The fabrication process starts with a thermal oxidation of the wafer and patterning of the oxide for the deep-silicon etching hard mask, followed by deep reactive ion etching (DRIE) of the handle wafer [see Fig. 4(b)] and subsequently of the device layer [see Fig. 4(c)]. The moving structures are free etched by wet etching of the buried oxide layer using hydrofluoric acid and critical point dryer to avoid stiction [see Fig. 4(d)]. A 1.0-μm-thick layer of gold is sputtered on both sides of the wafer using 50 nm of titanium tungsten as adhesion layer [see Fig. 4(e)]. At this step, both of the switching elements and the

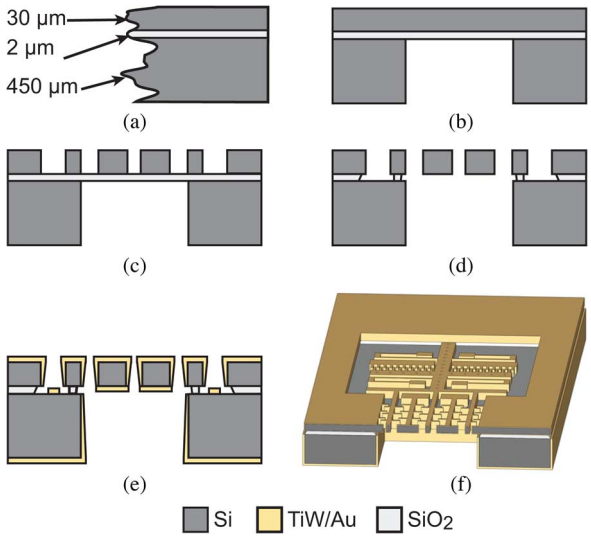

Fig. 4. SOI RF MEMS fabrication process of the waveguide switch and iris with reconfigurable surface. (a) SOI wafer. (b) DRIE of the handle wafer. (c) DRIE of the device layer. (d) Free etching of the moving structures by HF wet etching of the buried oxide layer. (e) Double-side metallization by sputtering. (f) 3D schematic cross-sectional view of the processed chip.

walls of the handle wafer are completely covered with gold. Different structural elements in the SOI device layer are electrically isolated by the previous underetching of the moving parts, which inhibits bridging of isolated islands in the device layer during the metal deposition due to the insufficient step coverage of the gold sputtering process.

Fig. 5 shows scanning electron microscope (SEM) images of a fabricated device, close-up views of the reconfigurable surface, and the metallization profile on the side walls of the vertical cantilevers, achieved with KDF 844NT metal sputter tool. The total chip size, including contact pads, handling areas and bias-line routing, is 15.30 mm $\times$ 3.70 mm with the MEMS area occupying a smaller fraction of 5.67 mm to 6.13 mm $\times$ 1.63 mm, depending on actuator implementation.

Fig. 6(a) shows an exploded 3-D schematic drawing of the measurement setup for mounting the chip into the waveguide, including the details of the tailor-made WR-12 flanges with recesses for chip self-alignment to the waveguide. For mounting the chips into the waveguide, a structured layer of Ted Pella Silver Conductive Sheet 16086 with nominal thickness of 125 μm and resistivity of 8 mΩ – cm is used only between the wide walls of the waveguide and device layer of the chip, leaving a gap between the surface of the narrower wall of the waveguide and the chip device layer, which allows for the mechanical feedthroughs through the narrower wall. It is not necessary to connect the narrower walls of the waveguide electrically to the chip, as the currents are mainly flowing on the top faces and a gap in the narrow walls up to hundreds of micrometer has no significant effect on the RF performance, as demonstrated by the authors previously [31].

A photograph of the RF measurement setup of the fabricated chips with reconfigurable surface integrated into WR-12 waveguide is shown in Fig. 6(b). The chips are fixed in the tailor-made flanges [Fig. 6(a)], which are connected to the millimeter-wave test heads with 1.0-mm coaxial outputs through V-band coaxial-to-waveguide adapters.

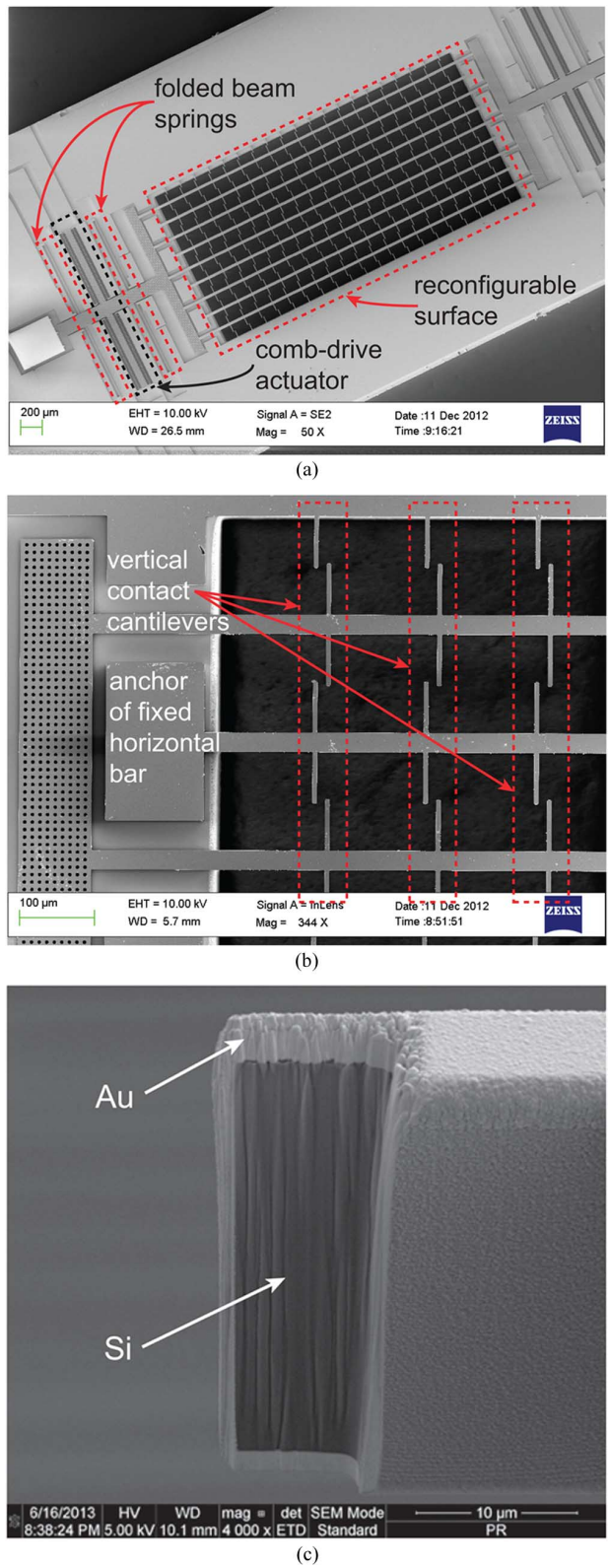

Fig. 5. SEM images of fabricated prototype devices. (a) Overview of the chip with one stage of comb-drive actuators with folded beam springs and reconfigurable surface. (b) Close-up view of the reconfigurable surface showing the vertical contact cantilevers and horizontal suspension bars. (c) Wafer cut showing the metal coverage on the side walls of the reconfigurable surface elements.

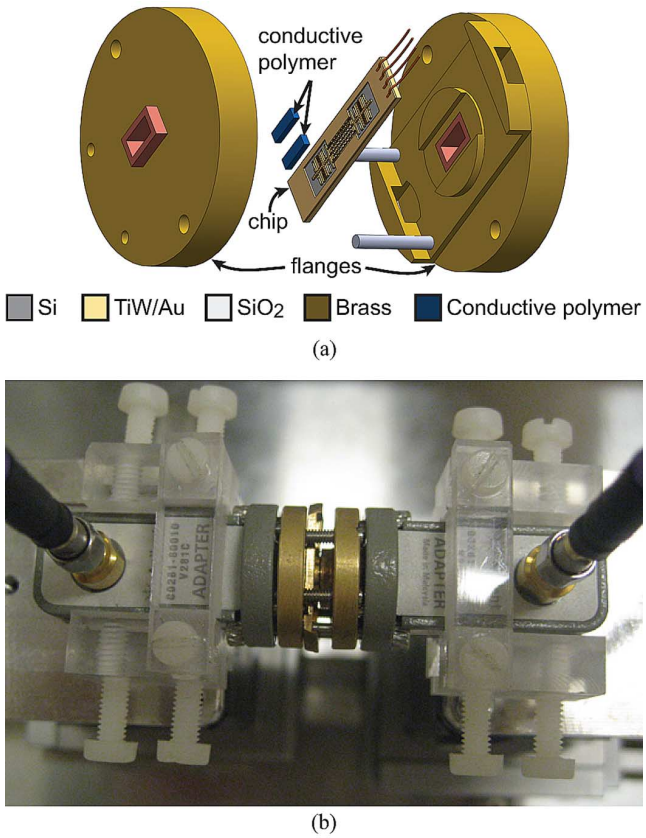

Fig. 6. Integration of the micromachined chips into a standard WR-12 waveguide and measurement setup. (a) Exploded 3-D schematic view of the integration into the waveguide. (b) Measurement setup with the chip integrated into the tailor-made flanges.

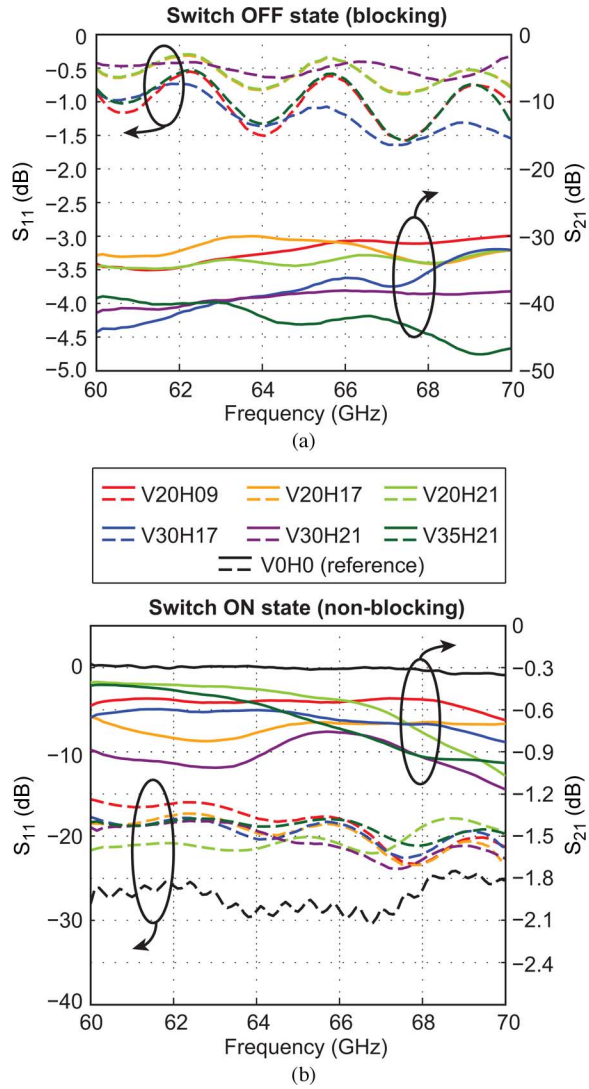

Fig. 7. S-parameter measurements of prototypes of the MEMS waveguide switches of the six primary designs with their design parameters listed in Table II, including a reference measurement on a dummy chip showing the losses of the setup (common legend to both sub-figures). (a) OFF state (blocking). (b) ON state (nonblocking).

V. Switch Characterization Results

A. RF Characterization

The RF measurements were performed using an Agilent E8361A vector network analyzer (VNA) with 110-GHz millimeter-wave test heads, calibrated using thru-reflect-line (TRL) calibration and a V-band waveguide calibration kit.

The calibration of the measurement setup is performed at the coaxial-to-waveguide adapters [see Fig. 6(b)]. Therefore, the measurements show the performance of the integrated chips combined with the tailor-made assembly setup, including the modified flanges and the polymer interposer. Reference measurements were carried out with the same assembly setup using a dummy chip, i.e., a chip fabricated in the same way as the waveguide switches, but only consisting of a micromachined waveguide frame without any MEMS elements on the chip.

Fig. 7 shows the measured RF performance of six waveguide-switch configurations, including a reference chip. The data includes losses by the chip-to-waveguide assembly based on two modified flanges and the polymer interposer, amounting to a total setup length of 30 mm between the calibration planes, including the waveguide flanges. The specification and dimensions of the reconfigurable surfaces measured here are the same as the ones simulated in Section III. The parameters of the six configurations are summarized in Table II. These configurations where chosen according to the expectations of the design study in Section III. The test chips contain either 20, 30, or 35 vertical columns (chip nomenclature Vxx), and either 9, 17, or 21 horizontal suspension bars (chip nominclature Hxx). These different implemented designs contain from 360 to 1470 vertical

TABLE II
Summary of Parameters of Waveguide Switches With the Performance Shown in Fig. 7

Design	Vertical columns	Horizontal bars	Contact cantilevers	Contact points
V20H09	20	09	360	200
V20H17	20	17	680	360
V20H21	20	21	840	440
V30H17	30	17	1024	540
V30H21	30	21	1260	660
V35H21	35	21	1470	770
V0H0 (reference)	0	0	-	-

cantilevers and between 200 and 770 parallel-actuated contact points.

No bias, i.e., actuation voltage, dependency was noticed during the measurements. Simulations indicate that electrical contact is actually not necessary between the cantilevers, as capacitive contact with gaps in the order of up to few tens of nanometers is sufficient, i.e., the performance in the blocking state was found not to be dependent on the contact force, contact resistance, and the number of cantilevers having physical contact.

In the OFF state (blocking), the three chips with 30 or 35 vertical columns have an isolation of 35–45 dB for the investigated frequency range of 60–70 GHz and thus perform better than the three chips with 20 vertical columns which have an isolation of 30–35 dB. This behavior is consistent with the expectations from the design study (Section III). The ON-state (nonblocking) insertion loss of all designs is between 0.4 and 1.1 dB for all devices over the whole frequency range, with the best performance of 0.4 dB measured for the V20H21 and V35H21 devices at 60 GHz. Device V20H9 has an overall best insertion loss, which is below 0.6 dB from 60 to 69 GHz. The reference chip reveals that the setup itself, including the chip mounting, polymer interposer, modified flanges for chip mounting, and standard flanges for connection to the waveguide adapters, attributes by about 0.3 dB to these losses, which is the major part of the losses of the best-performance measurements.

The ON-state return loss is between 15 and 25 dB for all devices over the 60–70-GHz frequency range. The reference chip has a return loss between 25–30 dB. The insertion loss of the waveguide switches presented in this paper is significantly better than PIN-diode based switches (2–6.5 dB) and, even including the losses of the waveguide prototype integration, does match very well the insertion loss of rotary motor switches (0.3–0.8 dB). The measured isolation is 10–20 dB better than PIN-diode-based waveguide switches and the designs with 30 and 35 vertical columns have an isolation equal to motor-driven rotary waveguide switches. Despite the operating frequency of the switches presented in this paper being 2–4× higher than for the previously published two MEMS waveguide switch implementations [27], [28], the insertion loss is significantly lower due to the low thickness of the MEMS reconfigurable surface of only 30 μm. Also, the isolation is higher by a factor of 2–3× despite the significantly higher operating frequency, which is achieved by the higher wave-blocking efficiency of the very dense vertical columns.

Linearity in both the ON and OFF states is expected to be very high since the device is actively kept in both states by a push–pull actuator. The calculated force in the end position is 23.64 and 46.20 μN for Designs A and B, respectively.

RF high-power handling performance of the MEMS waveguide switch could not be determined, as the power levels available to the authors in the V-band are limited to -19 dBm.

B. Electromechanical Characterization

The MEMS actuators comprise laterally-moving electrostatic comb-drives. The comb-drives are arranged in a push–pull configuration, and symmetrically placed to the left and the right of the narrow walls of the waveguide, as shown in Figs. 1 and 5(a).

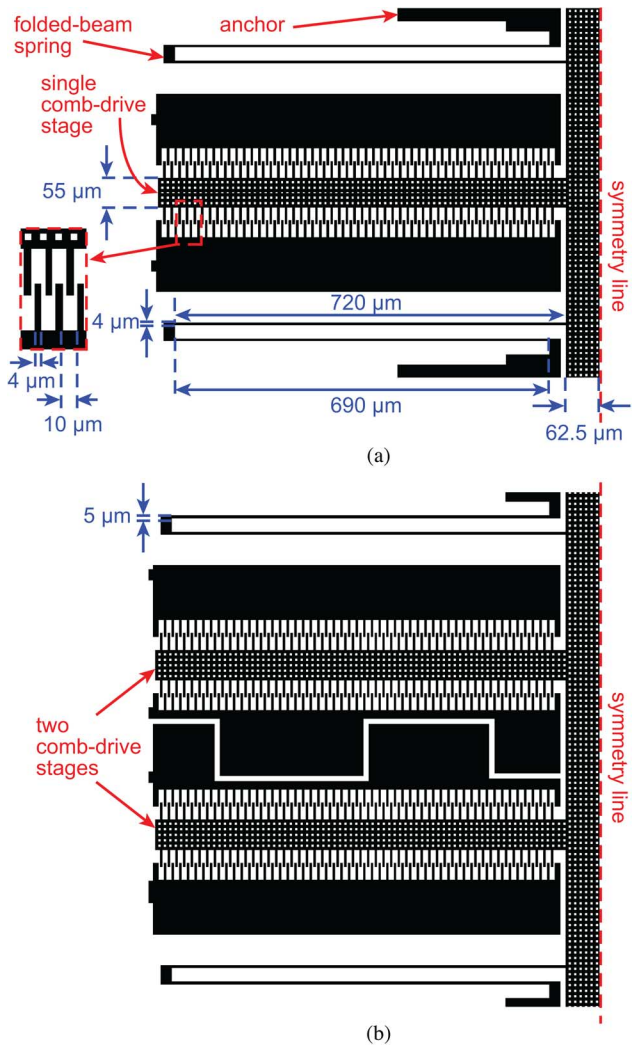

Fig. 8. Layouts with nominal dimensions of push–pull MEMS actuators. (a) Design A with a single electrostatic comb-drive stage. (b) Design B with two electrostatic comb-drive stages.

Fig. 8 shows the layouts of Design A with a single stage and Design B with two stages of electrostatic comb-drive push-pull actuators. For the fabricated devices, these stages are mirrored around the H-plane and E-plane of the waveguide, so that Designs A and B consist of a total of eight and 16 comb-drive actuators, respectively. The devices feature all-metal design, i.e., no dielectric layers are exposed to neither the RF field nor the dc (actuation) field, which virtually eliminates the reliability limitations by dielectric charging. Mechanical stoppers are implemented for limiting the actuator movements. Furthermore, due to the SOI RF MEMS device concept, all moving elements are utilizing monocrystalline silicon as the structural material, which provides high mechanical reliability. This silicon core is symmetrically metallized, which provides temperature compensation. As the device is bulk micromachined, there is no stress control/stress uniformity problems typical for surface micromachined MEMS devices. The mechanical spring has a spring constant of 1.97 N/m (actuator design A) or 3.85 N/m (actuator design B), which is relatively soft, but, in contrast to conventional MEMS switches, the spring is not used to provide a

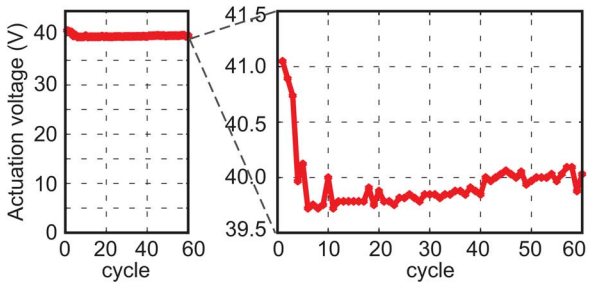

Fig. 9. Measured actuation voltage repeatability test for a chip with spring constant of 1.97 N/m and one stage of comb-drive actuators on each side of the reconfigurable surface.

restoring force but only to guide the movement of the actuator, as the device is actively pushed and pulled in both directions, i.e., features active opening and active closing. The total movement is 24 μm or ± 12 μm around the rest position. Fig. 9 shows the measured actuation voltage repeatability test for a chip with actuator design A, operated by a single-stage comb-drive with 106 fingers. After an initial 40 cycles of stabilization, the mean actuation voltage is 40.0 V with a standard deviation (1σ) of 0.0605 V for the 20 subsequent cycles. For our setup, the measurement of the switching speed was limited in resolution to the rise/fall time of the control signals, but it was confirmed that a single side actuation event is faster than 100 μs. The simulated passive release time for a critically damped case is 91 μs (10%–90% fall time), which corresponds to the simulated mechanical resonance frequency of 5.85 kHz for the actuator with spring constant of 1.97 N/m. However, the fact that the device is actively opened and actively closed allows for faster operation, in contrast to conventional MEMS transmission-line switches whose switching time is limited by the passive opening time and by design for critical damping. For instance, for a low-damped configuration with a mechanical Q-factor of 10 and an actuation voltage overdrive of 20% above the pull-in voltage, the full-swing actuation time is reduced to 29 μs according to dynamic simulations. It should be noted that this waveguide switch requires two actuation signals for its push–pull operation, and that the switching time also depends on the transition time between these two signals.

A chip with actuator design B and a two-stage comb-drive has a measured average actuation voltage of 44.13 V. This device was tested in continuous actuation in contact mode during 14 h, achieving 4.3 million cycles with a sawtooth input signal of 80 Hz, without noticing any degradation in performance or actuation voltage. The comb-drives are designed for high lateral robustness of 92 V (measured), giving a margin of at least a factor of two to the nominal actuation voltage. Actuation voltage overdrive may be done up to this voltage which sets the limit for the switching speed.

VI. Device-Level Yield Analysis

As the devices contain up to 1470 vertical cantilevers on a waveguide cross-sectional area of 3.1×1.55 mm^2, fabrication yield and random loss of vertical cantilevers due to the process yield is expected to have an influence on the RF performance

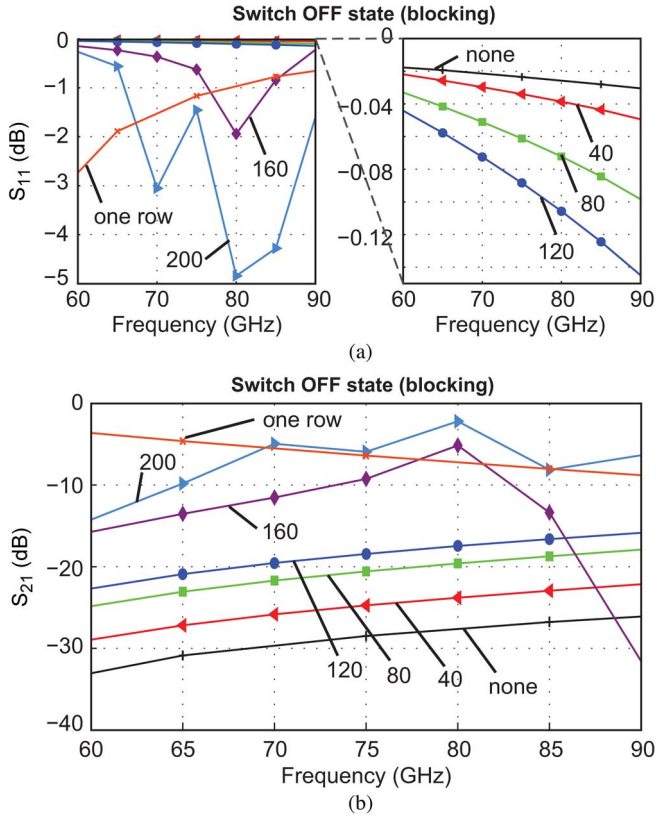

Fig. 10. HFSS-simulated device-level yield analysis of the MEMS waveguide switch with 20 vertical cantilever columns and 21 horizontal suspension bars in the OFF state: S-parameters for complete surface (100% yield), with 40 to 200 randomly selected cantilevers removed (95% to 76% yield), and for a complete central row of cantilevers removed. (a) S_{11}. (b) S_{21}.

in the blocking state. This is confirmed by the measured results of the first conference publication of the authors on this switch concept [30], which had a yield of 80%–85% and significantly worse RF performance than the devices in this paper. Fig. 10 shows an HFSS-simulated yield analysis for the design with uniformly distributed 20 vertical cantilever columns and 21 horizontal suspension bars in the OFF state. Losing a complete cantilever row close to the center of the waveguide decreases the isolation significantly to as low as 3.6–8.8 dB. The figure shows less drastic yield impact for 0–200 defective cantilevers randomly distributed over the array $(100\% - 76\%$ yield). For the loss of 120 cantilevers (86% yield), the isolation is reduced to 15.84–22.67 dB, which degrades this V20H21 design to the performance of a V10H21 design (Fig. 2). For measuring the effect of fabrication yield on the isolation of fabricated prototype devices, focused ion beam (FIB) milling was used to remove specific cantilevers in a controlled way. Fig. 11 shows a SEM picture of a cantilever array with two cantilevers removed. Fig. 12 shows the measured S-parameters for this yield analysis. Up to 200 cantilevers are removed in the same random pattern as simulated in Fig. 10. The measured results confirm, as predicted by simulation, that removing up to 120 contacts (86% yield) still achieves an isolation of better than 20 dB. For a yield of 95% (20 cantilever pairs removed), the measured isolation is 30 dB and close to the 100%-yield device with a measured isolation of 30–37 dB. For the RF

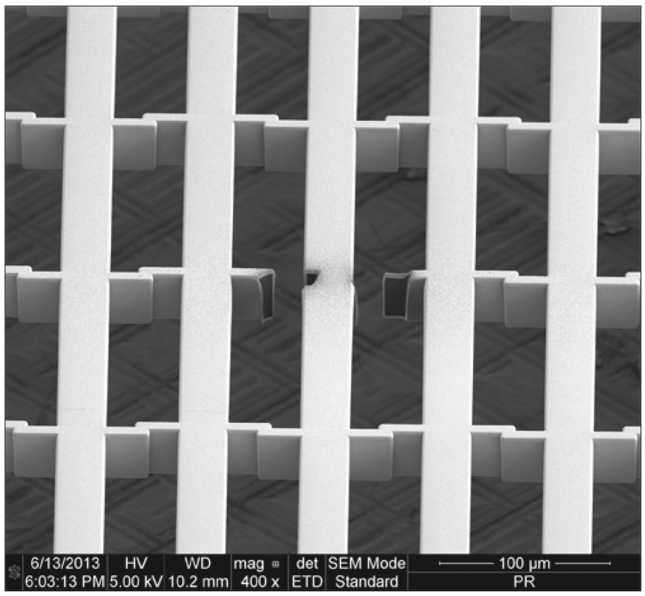

Fig. 11. Close-up SEM image of device for yield analysis, with two vertical contact cantilevers artificially removed by FIB milling. The gold-covered silicon core of the elements is revealed by the cut.

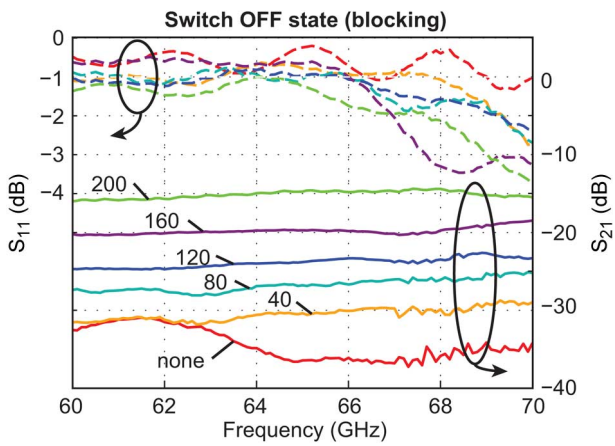

Fig. 12. Measured device-level yield analysis of switch S-parameter performance in the OFF state, of V20H21 devices with randomly removed cantilevers: 100% yield (no cantilever removed), and 95% yield (20 cantilever pairs removed) to 76% yield (100 cantilever pairs removed).

characterization in Section V, devices with 100% yield were selected.

VII. Reconfigurable Waveguide Iris

If the vertical cantilevers are only placed on specific areas of the waveguide cross section, other microwave structures such as MEMS-tunable waveguide irises are possible. Fig. 13 shows a simplified schematic view and a SEM picture of a fabricated tunable waveguide iris implemented with the presented MEMS-reconfigurable surface technology. In the ON state, the iris is active by short-circuiting the vertical cantilevers, and, in the OFF state, the iris is switched off by reconfiguring the surface to total transmission.

Fig. 14 shows the HFSS-simulated performance of the reconfigurable iris. For the ON state (iris active), it is compared with an ideal reference iris with filled metal areas. The distribution

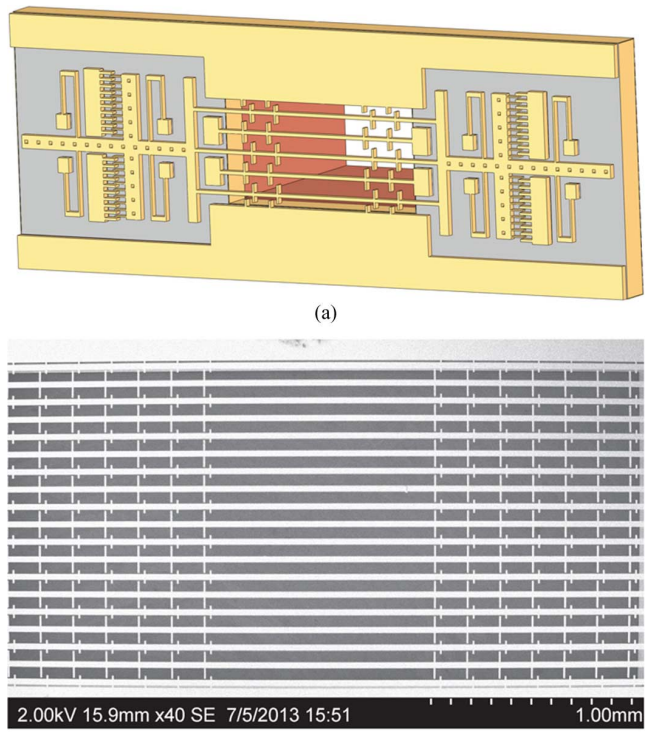

(a)

(b)

Fig. 13. MEMS-switchable waveguide iris based on reconfigurable surface. (a) Simplified schematic view (with iris OFF, i.e. fully transmissive). (b) SEM image of fabricated prototype device (iris OFF).

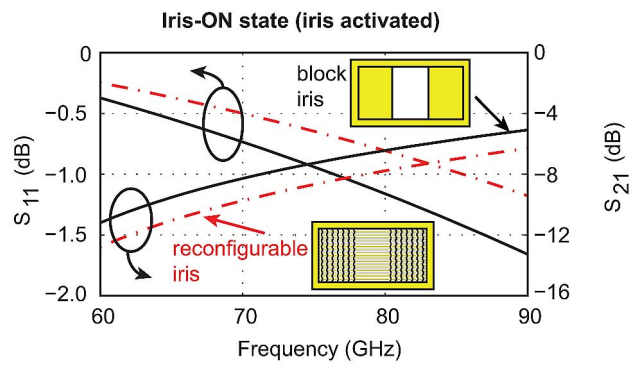

(a)

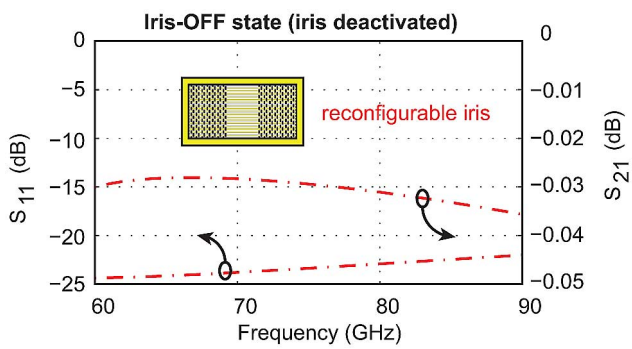

(b)

Fig. 14. HFSS-simulated performance of switchable inductive iris based on the MEMS reconfigurable surface with seven cantilever columns on each side of the opening. (a) Iris switched ON (columns short-circuited) and comparison to ideal iris. (b) Iris switched OFF.

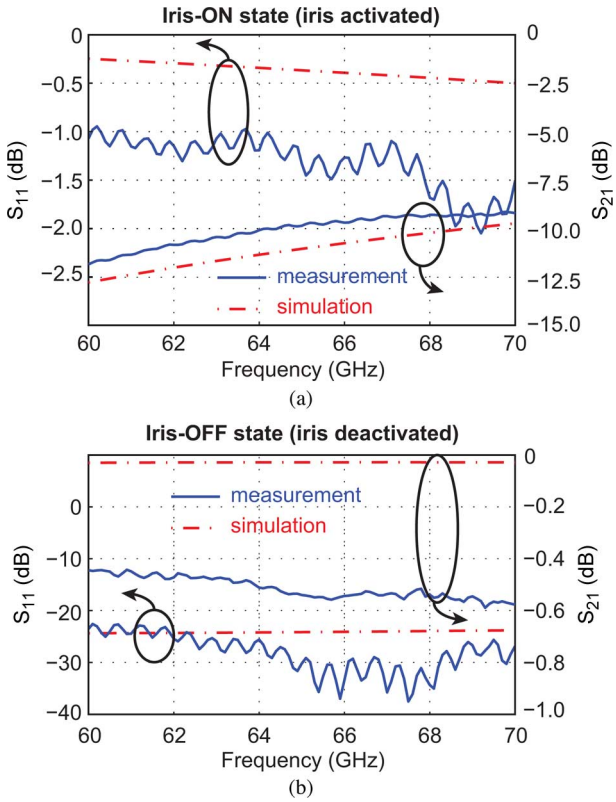

Fig. 15. Measured S-parameters of prototype device implemented as MEMS-reconfigurable inductive iris. (a) Iris switched ON. (b) Iris switched OFF.

of the cantilever columns is the same as the uniform switch design with 20 vertical cantilever columns and 17 horizontal suspension bars, where six of the cantilever columns in the middle of the waveguide are removed, while keeping seven cantilever columns on each side, keeping all other parameters similar to the switch designs. The resulting iris opening is 1.075 mm in the WR-12 waveguide frame. Measurement results of a fabricated reconfigurable iris is shown in Fig. 15. In the iris OFF state (iris deactivated), the device exhibits an insertion loss of 0.4–0.6 dB (including the measurement setup losses of 0.3–0.4 dB) and return loss of better than 22 dB over the 60–70-GHz frequency range. For the iris in the ON state (iris activated), the device shows S_{11} of -1 to -2 dB and S_{21} of -9 to -12 dB. The measured values are in good agreement with the simulated ones, except for the insertion loss, which is similar to the waveguide switches, primarily impacted by the setup losses.

VIII. Conclusion

This paper reported on an SPST rectangular waveguide switch based on a fully functional 30-μm-thick reconfigurable MEMS surface which consists of up to 1470 elements with 660 contact points, integrated in a standard WR-12 waveguide. The devices comprise the first MEMS waveguide switches above 40 GHz. The measurement results confirmed that the isolation is better than 30 dB for all designs and the insertion loss is better than 0.65 dB for the best design for the whole frequency range from 60 to 70 GHz. The major part of the insertion loss is attributed to the measurement setup which contributes up to 0.3 dB. These devices have similar performance as rotary motor-based waveguide switches, but have a drastically reduced size, and perform significantly better in microwave performance than commercial PIN-diode waveguide switches. A device-level yield analysis based on simulations and measurements of manipulated devices was presented which showed that a 95% fabrication yield is sufficient for achieving close-to best performance. Furthermore, a MEMS-reconfigurable 60–70-GHz waveguide iris based on the MEMS-reconfirugable surface was presented, and simulation and measurement results were shown.

Acknowledgment

The authors would like to thank U. Shah, KTH Royal Institute of Technology, Stockholm, Sweden, for help with the fabrication of microchips, and J. Åberg, MicroComp Nordic AB, Stockholm, Sweden, for fabrication of tailor-made flanges for the measurement setup, as well as N. Chekurov for assistance with the focused-ion-beam milling. Furthermore, the help of K. Noren, KTH Royal Institute of Technology, with the fabrication of chip holders for critical point dryer and metal sputterer, is highly appreciated.

References

[1] Y. Choung, "V-band crosslink antenna," in *Proc. IEEE Antennas Propag.*, Jul. 2005, vol. 3A, pp. 387–390.
[2] G. Chan and F. Razaqpur, "Spectrum requirements of an indoor pico-cell radio system," *IEEE Trans. Veh. Technol.*, vol. 44, no. 1, pp. 24–30, Jan. 1995.
[3] P. Smulders, "Exploiting the 60 GHz band for local wireless multimedia access: Prospects and future directions," *IEEE Commun. Mag.*, vol. 40, no. 1, pp. 140–147, Jan. 2002.
[4] V. Dyadyuk, Y. Guo, and J. Bunton, "Multi-gigabit wireless communication technology in the E-band," *IEEE Wireless VITAE*, pp. 137–141, May 2009.
[5] J. Wenger, "Automotive radar—Status and perspectives," in *Proc. IEEE Compound Semicond. Integr. Circuit Symp.*, Oct. 2005, pp. 21–24.
[6] J. A. Nanzer, *Microwave and Millimeter-Wave Remote Sensing for Security Applications*. Norwood, MA, USA: Artech House, 2012.
[7] I. McAuley, L. Young, M. Gradziel, W. Lanigan, C. O'Sullivan, J. Murphy, R. Mahon, R. May, and N. Trappe, "Millimetre-wave and terahertz imaging systems with medical applications," in *Proc. Infrared Millimeter Waves and 14th Int. Conf. Terahertz Electron.*, Sep. 2006, pp. 371–371.
[8] F. Topfer, S. Dudorov, and J. Oberhammer, "Micromachined 100 GHz near-field measurement probe for high-resolution microwave skin-cancer diagnosis," in *IEEE MTT-S Int. Microw. Symp. Dig.*, Jun. 2012, pp. 1–3.
[9] H. H. Meinel, "Millimeter wave applications and technology trends," *Ann. Telecommu.*, vol. 47, no. 11–12, pp. 456–468, 1992.
[10] M. Marcus and B. Pattan, "Millimeter wave propagation; spectrum management implications," *IEEE Microwave*, vol. 6, no. 2, pp. 54–62, 2005.
[11] V. Lubecke, K. Mizuno, and G. Rebeiz, "Micromachining for terahertz applications," *IEEE Trans. Microw. Theory Techn.*, vol. 46, no. 11, pp. 1821–1831, Nov. 1998.
[12] E. Hettlage and G. Ruff, "Rotary Waveguide Switch Having Arcuate Waveguides Realized by Planar Faces," U.S. Patent 4 967 170A, 1990.
[13] R. B. Greed, "Waveguide Switch," EP Patent 0 399 739 A2, Nov. 28, 1990.
[14] G. M. Rebeiz, *RF MEMS Theory, Design and Technology*, 1st ed. Hoboken, NJ, USA: Wiley, 2003.
[15] V. K. Varadan, K. J. Vinoy, and K. A. Jose, *RF MEMS and Their Applications*. Chichester, U.K.: Wiley, 2003.
[16] C. Patel and G. Rebeiz, "A high-reliability high-linearity high-power RF MEMS metal-contact switch for DC-40-GHz applications," *IEEE Trans. Microw. Theory Techn.*, vol. 60, no. 10, pp. 3096–3112, Oct. 2012.

[17] D. Mercier, P. Charvet, P. Berruyer, C. Zanchi, L. Lapierre, O. Vendier, J. Cazaux, and P. Blondy, "A DC to 100 GHz high performance ohmic shunt switch," in *IEEE MTT-S Int. Microw. Symp. Dig.*, June 2004, vol. 3, pp. 1931–1934.
[18] B. Ghodsian, P. Bogdanoff, and D. Hyman, "Wideband DC-contact MEMS series switch," *IET Micro Nano Lett.*, vol. 3, no. 3, pp. 66–69, 2008.
[19] F. Solazzi, C. Palego, D. Molinero, P. Farinelli, S. Colpo, J. Hwang, B. Margesin, and R. Sorrentino, "High-power high-contrast RF MEMS capacitive switch," in *Proc. IEEE Eur. Microw. Int. Circuits Conf.*, Oct. 2012, pp. 32–35.
[20] T. M. Vu, G. Prigent, J. Ruan, A. Rumeau, P. Pons, and R. Plana, "Fabrication and characterization of RF-MEMS switch in V-band," in *Proc. Asia–Pacific Microw. Conf.*, Dec. 2009, pp. 202–205.
[21] J. Rizk, G.-L. Tan, J. B. Muldavin, and G. Rebeiz, "High-isolation W-band MEMS switches," *IEEE Microw. Wireless Compon. Lett.*, vol. 11, no. 1, pp. 10–12, Oct. 2001.
[22] J. B. Rizk and G. Rebeiz, "W-band CPW RF MEMS circuits on quartz substrates," *IEEE Trans. Microw. Theory Techn.*, vol. 51, no. 7, pp. 1857–1862, Jul. 2003.
[23] L. Larson, R. Hackett, and R. Lohr, "Microactuators for GaAs-based microwave integrated circuits," in *Proc. Transducers Conf.*, Jun. 1991, pp. 743–746.
[24] S. Majumder, J. Lampen, R. Morrison, and J. Maciel, "A packaged, high-lifetime ohmic MEMS RF switch," in *IEEE MTT-S Int. Microw. Symp. Dig.*, Jun. 2003, vol. 3, pp. 1935–1938.
[25] J. Muldavin and G. Rebeiz, "Inline capacitive and DC-contact MEMS shunt switches," *IEEE Microwave Wireless Compon. Lett.*, vol. 11, no. 8, pp. 334–336, Aug. 2001.
[26] T. Seki, S. Sato, T. Masuda, I. Kimura, and K. Imanaka, "Low-loss RF MEMS metal-to-metal contact switch with CSP structure," in *Proc. Transducers Conf.*, Jun. 2003, vol. 1, pp. 340–341.
[27] M. Daneshmand, R. Mansour, and N. Sarkar, "RF MEMS waveguide switch," *IEEE Trans. Microw. Theory Techn.*, vol. 52, no. 12, pp. 2651–2657, Dec. 2004.
[28] M. Daneshmand and R. Mansour, "Multiport MEMS-based waveguide and coaxial switches," *IEEE Trans. Microw. Theory Techn.*, vol. 53, no. 11, pp. 3531–3537, Nov. 2005.
[29] M. Sterner, N. Roxhed, G. Stemme, and J. Oberhammer, "Static zero-power-consumption coplanar waveguide embedded DC-to-RF metalcontact MEMS switches in two-port and three-port configuration," *IEEE Trans. Electron Devices*, vol. 57, no. 7, pp. 1659–1669, Jul. 2010.
[30] Z. Baghchehsaraei, U. Shah, S. Dudorov, G. Stemme, J. Oberhammer, and J. Aberg, "MEMS 30- μm-thick W-band waveguide switch," in *Proc. IEEE Eur. Microw. Conf.*, Oct. 2012, pp. 1055–1058.
[31] Z. Baghchehsaraei, U. Shah, J. Åberg, G. Stemme, and J. Oberhammer, "MEMS reconfigurable millimeter-wave surface for V-band rectangular waveguide switch," *Int. J. Microw. Wireless Technol.*, vol. 5, no. 3, pp. 341–349, Jun. 2013.
[32] Z. Baghchehsaraei, U. Shah, J. Aberg, G. Stemme, and J. Oberhammer, "Millimeter-wave SPST waveguide switch based on reconfigurable MEMS surface," in *IEEE MTT-S Int. Microw. Symp. Dig.*, Jun. 2013, pp. 1–3.
[33] G. Rebeiz, C. Patel, S. Han, C.-H. Ko, and K. Ho, "The search for a reliable MEMS switch," *IEEE Microwave*, vol. 14, no. 1, pp. 57–67, 2013.
[34] C. Goldsmith, J. Maciel, and J. McKillop, "Demonstrating reliability," *IEEE Microwave*, vol. 8, no. 6, pp. 56–60, 2007.
[35] M. Sterner, N. Somjit, U. Shah, S. Dudorov, D. Chicherin, A. Räisänen, and J. Oberhammer, "Microwave MEMS devices designed for process robustness and operational reliability," *Int. J. Microw. Wireless Technol.*, vol. 3, no. 5, pp. 547–563, Oct. 2011.
[36] R. E. Collin, *Foundation for Microwave Engineering*, 2nd ed. New York, NY, USA: McGraw-Hill, 1992.

Zargham Baghchehsaraei (S'12) was born in Tehran, Iran, in 1982. He received the B.S. degree from the Iran University of Science and Technology, Tehran, Iran, in 2006, and the M.S. degree from the Chalmers University of Technology, Gothenburg, Sweden, in 2009, both in electrical engineering. He is currently working toward the Ph.D. degree at the Department of Micro and Nanosystems (MST), KTH Royal Institute of Technology, Stockholm, Sweden, under the supervision of Dr. J. Oberhammer.

His research focus includes microwave and RF MEMS-based switches, phase shifters, filters, and antenna arrays.

Mr. Baghchehsaraei was a Student Paper Competition finalist at the IEEE International Microwave Symposium, Seattle, WA, USA, June 2013, and the recipient of the Best Poster Award presented at the Micromechanics and Microsystems Europe Workshop, Espoo, Finland, September 2013.

Joachim Oberhammer (SM'12) was born in Italy in 1976. He received the Ph.D. degree from KTH Royal Institute of Technology, Stockholm, Sweden, in 2004.

In 2007, he became an Associate Professor with the Royal Institute of Technology, Stockhom, Sweden, where he is heading a research team with activities in RF and microwave MEMS. In 2007, he was a Research Consultant with Nanyang Technological University, Singapore, and, in 2008, he was a Guest Researcher with Kyoto University, Kyoto, Japan. He is the author and coauthor of more than 100 reviewed research papers and holds four patents.

Dr. Oberhammer has been a Steering Group member of the IEEE Microwave Theory and Techniques Society (MTT-S) and Antennas and Propagation Society (AP-S) Chapters Sweden since 2009. In 2004, he received an Ericsson Research Foundation Award and in 2007 a grant by the Swedish Innovation Bridge. In 2008, he received a scholarship from the Japanese Society for the Promotion of Science. Since 2009, the research work he is heading received four Best Paper Awards, an Honorable Mention, and three Graduate Fellowships of the IEEE MTT-S and AP-S. He served as a TPRC member of the IEEE Transducers Conference 2009, the IEEE International MTT-S Microwave Symposium 2010–2014, and the IEEE Micro Electromechanical Systems 2011 and 2012.